


Raman mode softening in SrMnO₃ induced by optical excitationArup Kumar Mandal,¹ Aprajita Joshi²,³ Surajit Saha,² Binoy Krishna De,¹ Sourav Chowdhury,¹ V. G. Sathe,¹ U. Deshpande,¹ D. Shukla,¹ Amandeep Kaur³,⁴ D. M. Phase,¹ and R. J. Choudhary^{1,*}¹*UGC-DAE Consortium for Scientific Research, Indore-452001, Madhya Pradesh, India*²*Department of Physics, Indian Institute of Science Education and Research, Bhopal 462066, India*³*Department of Physics, Indian Institute of Technology Bombay, Powai, Mumbai 400076, India* (Received 20 May 2022; revised 4 July 2022; accepted 15 August 2022; published 9 September 2022)

In recent years, photosensitive materials have been in huge demand because of their fascinating ability to convert absorbed photon energy to generate strain and henceforth tuning physical properties. In this work we report the photosensitive activity of SrMnO₃. Using a power-dependent and temperature-dependent Raman study with different laser sources having wavelengths across the optical band gap of SrMnO₃, we divulge the photosensitive character of SrMnO₃ thin film. Upon laser light illumination, Raman modes soften, and softening increases further with an increase in laser power. A similar kind of mode variation is observed with increasing temperature at fixed laser power. A soft x-ray absorption near-edge structure in the presence of laser illumination reveals the change in crystal field splitting associated with mode softening.

DOI: [10.1103/PhysRevB.106.104104](https://doi.org/10.1103/PhysRevB.106.104104)

Introducing strain in cross-functional materials and tuning their physical properties have been generating huge interest among materials scientists in recent years [1–4]. Among several ways of inducing strain in multifunctional materials, photoinduced strain has been attracting huge attention because of its easy switching ability between strain and the relaxed state [5]. Among various perovskite-based compounds, only a few halide- and oxide-based systems have shown photosensitive distortion [6–21]. Particularly in transitional metal oxide series, this phenomenon is restricted in only a few ferroelectric and multiferroic systems [7,13,20]. The microscopic origin of change in the physical properties of materials with light illumination is still not clear even for very common photostrictive materials [7]. This uncertainty arises because there is no one-to-one correspondence between the optical photon energy being used to induce photostrictive effects with the spin-orbit interaction energy of three-dimensional (3D) transition metal system in its ground state, although natural vibrational frequency of the perovskite systems is much smaller than the optical vibration frequency of light. In photosensitive systems, absorbed photon energy causes changes in the materials' ground state via a secondary process such as the photovoltaic effect or inverse piezoelectric effect [7]. In such processes, a variation in local temperature upon photon absorption plays a crucial role, which can also lead to changes in the materials' ground state. For instance, local temperature-assisted distortion can also modulate different physical properties of the system via variation in the electronic structure, available exchange interactions, hopping of the carriers, etc.

In this work, we introduce SrMnO₃ as a photosensitive material. In transition metal perovskite series, SrMnO₃ is a

very promising one, particularly in thin-film form, owing to its recently reported multiferroic, giant magnetocaloric character, which can be induced under certain strain configurations [22–27]. For the past decade, several interesting theoretical and experimental reports have been presented on thin-film structures of SrMnO₃ [22–27]; however, photoinduced effects on structural and physical properties of this material have not yet been explored. We performed power-dependent Raman measurements (with a 473-nm, 532-nm, and 633-nm laser source) across the optical band gap of hexagonal strontium manganite (4H-SMO) thin film grown on an optically transparent quartz substrate. We observed changes in *p-d* hybridization with changes in crystal field values when SMO is illuminated with a 532-nm and 633-nm light source.

I. EXPERIMENTAL

4H-SMO thin film was grown on an optically transparent quartz substrate using the pulsed laser deposition technique (KrF excimer laser, $\lambda = 248$ nm) with a dense pellet of single-phase 4H-SMO as the target. The preparation procedure for 4H-SMO is described elsewhere [25]. During thin-film deposition, we maintained the oxygen partial pressure at 120 mTorr and the substrate temperature at 700 °C. The structural single-phase nature of the grown film was confirmed by grazing incident x-ray diffraction (GIXRD) using a Bruker D8-Discover high-resolution x-ray diffractometer with an incident θ value of 0.5° (see Supplemental Material [28]), which also revealed its polycrystalline character (Supplemental Material Fig. S1 [28]). The diffraction pattern and calculated lattice parameters are shown in Supplemental Material Fig. S1 [28]. Surface morphology and related information are extracted from Atomic Force Microscopy (AFM) measurements, performed in contact mode (Supplemental Material Fig. S1 [28]), as discussed in the Supplemental Material [28].

*Corresponding author: ram@csr.res.in

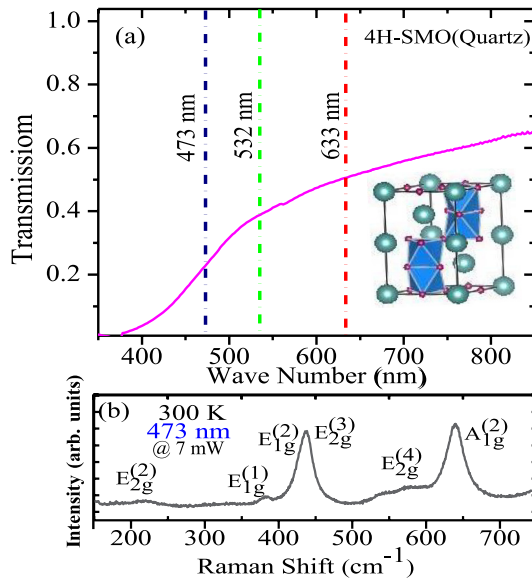


FIG. 1. (a) UV-Vis spectra of 4H-SMO thin film on quartz (in transmission mode). (b) Raman spectra of 4H-SMO thin film with a 473-nm laser source at room temperature (300 K).

X-ray photoemission spectroscopy measurements were performed to confirm the chemical purity of the grown film using an Omicron energy analyzer (EA-125 Germany) with an Al K_{α} (1486-eV) x-ray source (see Supplemental Material [28]). The thickness of the grown film is calculated from x-ray reflectivity measurements and is around 45 nm (Supplemental Material Fig. S2 [28]).

Power-dependent Raman measurements were performed with a 473-nm, 532-nm, and 633-nm laser source at 300 K and 150 K. Power-dependent and temperature-dependent Raman measurements with a 473-nm laser source was done by Horiba JY make HR-800 Raman instruments (spot diameter, 1 μm). Power-dependent Raman spectra with 532-nm and 633-nm laser sources with a spot diameter of 1 μm were collected with a LabRAM HR Evolution Raman spectrometer in the backscattering geometry equipped with a Peltier-cooled charge-coupled device as the detector. The sample temperature was varied using a Linkam heating stage (model HFS600E-PB4). Soft x-ray absorption near-edge structure experiments were performed across the Mn-L edge and the O-K edge of 4H-SMO film, along with MnO_2 and Mn_2O_3 reference samples with and without 532-nm and 633-nm light illumination at room temperature (300 K) in total electron yield mode at beamline BL-01, Indus-2, RRCAT, India. During x-ray absorption (XAS) measurements, we illuminated our sample with a 532-nm and 633-nm laser light at an incident angle of 45° to the normal of the sample surface. The XAS measurements were done using a JD-303 laser source with a power density of $166 \text{ mW}/\text{mm}^2$.

II. RESULTS AND DISCUSSION

Figure 1(a) represents the Ultra Violet-visible spectra (UV-Vis in transmission mode) of the grown film. The calculated band gap (direct band gap calculated from the Tauc plot) of the grown film is 2.5 eV ($\sim 495 \text{ nm}$) (see Supplemental

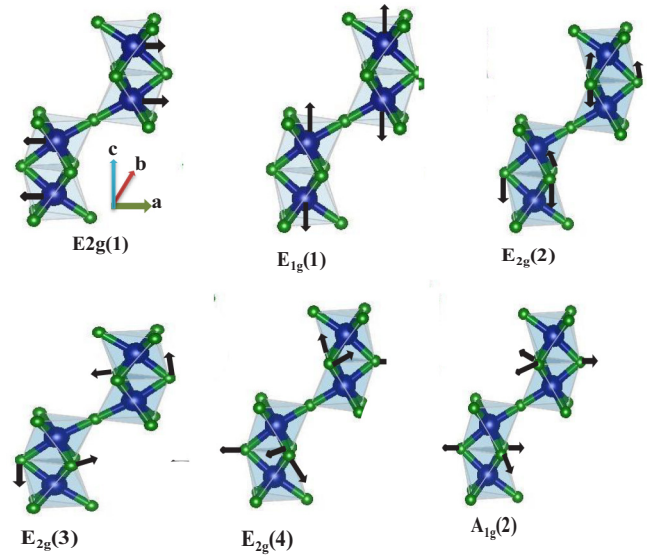


FIG. 2. Schematic of allowed vibrational mode of 4H-SMO.

Material [28]). Figure 1(b) represents the room-temperature (300 K) Raman spectrum of the grown 4H-SMO film recorded with the 473-nm laser source. All vibration modes are assigned according to space group symmetry and results of previous studies [25,29,30]. In 4H-SMO, 1-unit cell consists of 4 MnO_6 octahedra, which form two Mn_2O_9 bioctahedra by three face-sharing oxygens. Two bioctahedra in a unit cell are connected through Mn—O—Mn 180° bonding [31]. Closer inspection reveals that the Mn_2O_9 bioctahedra consist of two types of oxygen: face-sharing oxygen (O1) and corner-sharing oxygen (O2) (Fig. 2). In 4H-SMO, only face-sharing oxygen (O1) is Raman active [25,30]. According to group theory, eight vibrational modes are allowed in the 4H-SMO structure ($\Gamma = 2A_{1g} + 2E_{1g} + 4E_{2g}$). Out of eight vibrational modes, only six single phonon modes are prominent for 4H-SMO (Fig. 2). Details of the observed modes for 4H-SMO are described elsewhere [25]. In Fig. 1(b), the $A_{1g}^{(2)}$ (A_g) mode at around 640 cm^{-1} represents O1 displacement in Mn_2O_9 bioctahedra. In both power-dependent and temperature-dependent Raman studies (see Supplemental Material [28]), we observe softening of the A_g mode at around 640 cm^{-1} as well as the E_g mode at 435 cm^{-1} . However, shifting of the E_g mode toward a lower frequency site is quite lower than the A_g mode shift (E_g mode softening with different laser sources and temperatures is highlighted in Supplemental Material Figs. S6–S8 [28]). Some of the lower frequency E_g modes (382 cm^{-1} , 220 cm^{-1}) remain invariant with respect to laser power or temperature. For this reason, we have focused our analysis based on A_g mode variation with respect to different laser power and temperature with a 473-nm, 532-nm, and 633-nm laser source.

Figure 3(a1) represents a power-dependent variation of the A_g mode with the 473-nm laser source at 150 K. Figure 3(a2) represents a 3D intensity contour of Fig. 3(a1) data. From both the two-dimensional and 3D plots, it is revealed that with increasing laser power, A_g mode shifts toward a lower frequency by up to 5.7 cm^{-1} . Besides the A_g mode softening, it is also clear from the 3D plot that the broadening of the A_g mode increases with increasing laser power. Figures 3(b1)

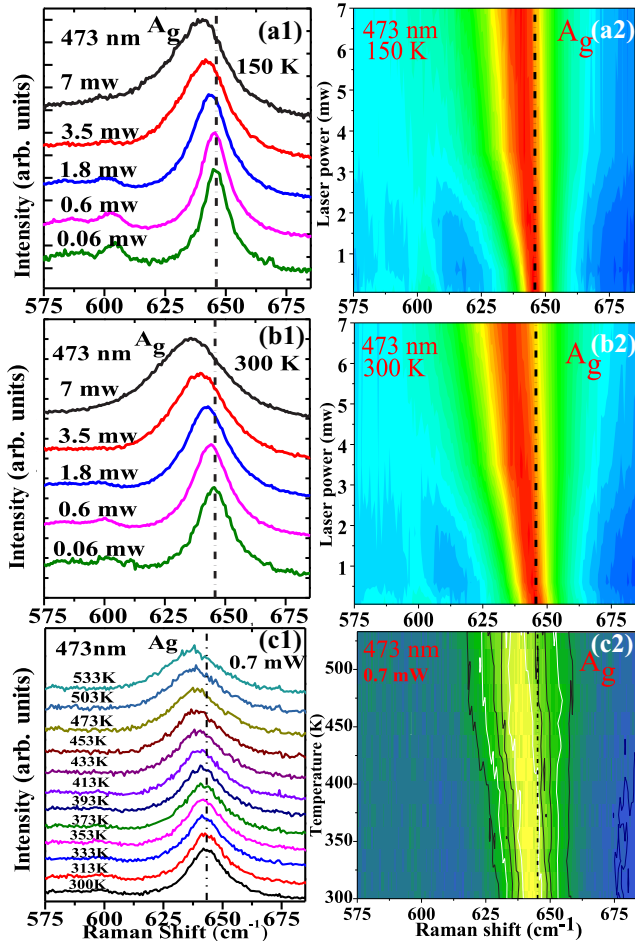


FIG. 3. (a1), (a2) Power-dependent variation of the A_g mode of SMO film at 150 K with a 473-nm laser source. (a2) Intensity contour plot of (a1). (b1), (b2) Power-dependent variation of the A_g mode at 300 K with a 473-nm laser source. (c1), (c2) Temperature-dependent variation of the A_g mode with a 473-nm laser source at fixed 0.7-mW laser power (full spectra are available in Supplemental Material [28]).

and 3(b2) represent the power-dependent variation of the A_g mode position and its intensity contour plot, respectively, with a 473-nm laser source at 300 K. (Full Raman spectra are available in Supplemental Material Fig. S3(b) [28]). From both Figs. 3(b1) and 3(b2), it is clear that with increasing laser power, A_g mode softening takes place along with broadening, similar to the observations at 150 K. Figure 3(c1) and 3(c2) represents the variation of the A_g mode with temperature recorded, with a 473-nm laser source at 0.7 mW, which also reveals A_g mode softening with increasing temperature. (Full Raman spectra are available in Supplemental Material Fig. S3(c) [28]). From room temperature (300 K) to 533 K, A_g mode shifts by 6.4 cm^{-1} toward a lower frequency at a fixed laser power.

We also carried out a similar exercise with a laser source of 532 nm as well as 633 nm at different temperature values and varying laser power, and observed variation in the A_g mode. Figure 4 represents the power-dependent (at 150 K and 300 K) and temperature-dependent full Stokes and anti-Stokes Raman spectra with the 532-nm laser source. Similar mode softening is observed at room temperature (300 K) as well

as at 150 K, and the overall change in frequency (A_g mode) between minimum and maximum laser power with a 532-nm laser source is 7.9 cm^{-1} at 300 K and 7.3 cm^{-1} at 150 K, and at a fixed 1.69-mW laser power, it is softened by a 7.1-cm^{-1} shift as the temperature is increased from 300 K to 700 K. Details of A_g mode softening with varying laser power and with varying temperature are highlighted in Supplemental Material Fig. S4 [28] with a contour plot. Figure 5 represents power-dependent (at 150 K and 300 K) and temperature-dependent full Stokes and anti-Stokes Raman spectra with a 633-nm laser source. With the 633-nm laser source, A_g mode softens by 10.1 cm^{-1} at 150 K and 10.3 cm^{-1} at 300 K between the minimum and maximum laser power, whereas at a fixed 2.87-mW laser power, it softens by 10.3 cm^{-1} with an increase in temperature from 300 K to 700 K. Details of A_g mode softening with varying laser power and with varying temperature are highlighted in Supplemental Material Fig. S5 [28] with a contour plot. For both laser sources, softening of the A_g mode takes place with increasing laser power along with increasing broadening of mode, similar to the temperature-dependent A_g mode variation at a fixed laser power. It is noted here that the local structure modification (softening of the A_g mode) obtained with 9-mW laser illumination (with 532 nm and 633 nm) is similar to the distortion (softening of the A_g mode) obtained via a substrate-induced strain of $\sim 1.2\%$ in this structure [25].

Overall, Raman measurements reveal that the most intense A_g mode of 4H-SMO shifts toward the lower frequency side with an increasing laser power of the 473-, 532-, and 633-nm laser source. The A_g mode exhibits similar variation with increasing temperature at a fixed laser power with the 473-, 532-, and 633-nm laser source. These observations are suggestive of a local rise in temperature of 4H-SMO in a power-dependent Raman shift. For a better understanding of the power-dependent Raman shift with the effect of local temperature, we analyzed both the Stokes and anti-Stokes Raman line with different power and temperature using 532 nm and 633 nm. One can calculate the local temperature by the intensity ratio of the Stokes and anti-Stokes line with the following equation [7]:

$$\frac{I_S}{I_{AS}} = \frac{(\vartheta_{\text{excitation}} - \vartheta_{\text{phonon}})^3}{(\vartheta_{\text{excitation}} + \vartheta_{\text{phonon}})^3} \exp^{h\vartheta_{\text{phonon}}/KT},$$

where I_S is the intensity of the Stokes line, I_{AS} is the intensity of anti-Stokes line, $\vartheta_{\text{excitation}}$ is the frequency of the excitation laser, $\vartheta_{\text{excitation}} - \vartheta_{\text{phonon}}$ is the frequency of the Raman anti-Stokes line, and $\vartheta_{\text{excitation}} + \vartheta_{\text{phonon}}$ is the frequency of the Raman Stokes line. Accordingly, we calculated local temperature for all the spectra taken with different power and temperature, with a 532-nm and a 633-nm laser source, and plot them together to probe the variation of the A_g mode as shown in Figs. 6(a) and 6(b), respectively. We also took into account the laser power-induced heating effect in temperature-dependent measurements for each temperature scan, so all the data points in Fig. 6 are in thermal equilibrium. From Fig. 6(a), it is clear that when the spectrum is recorded at 150 K with a 532-nm laser at the highest available power (16.10 mW), the local temperature increases up to 740 K. The trend of the power-dependent A_g mode shift at 150 K

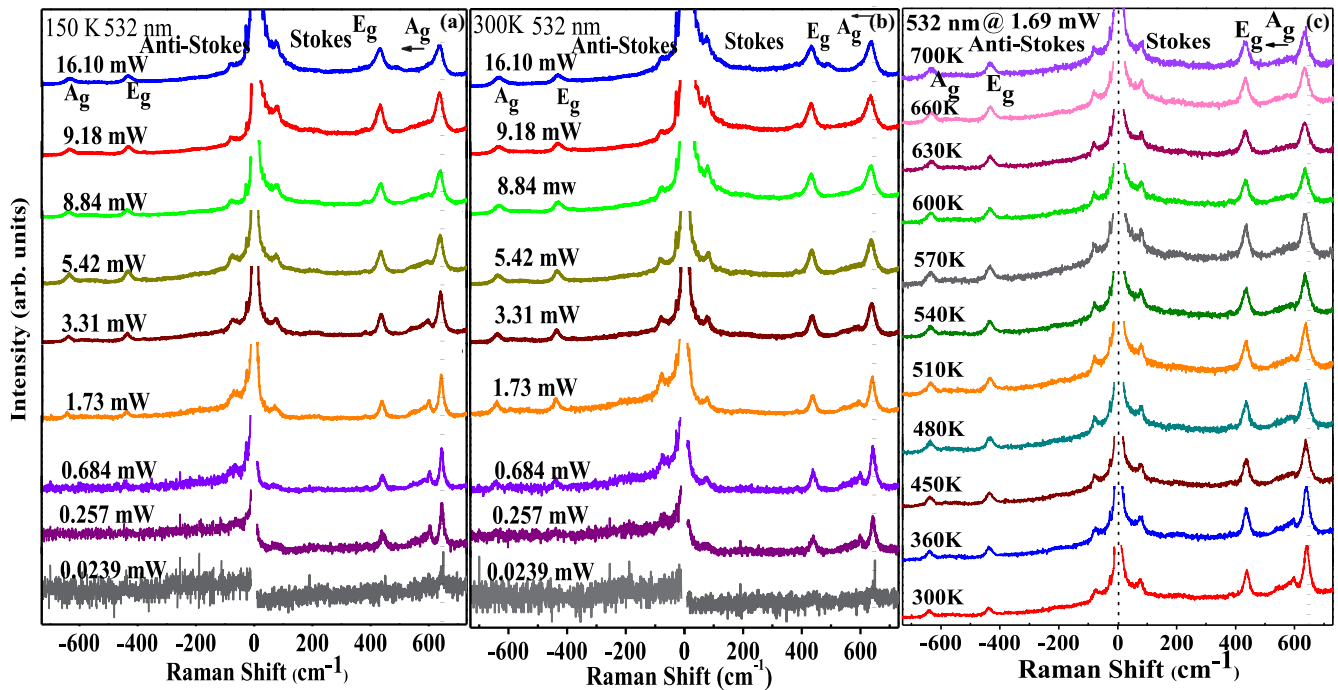


FIG. 4. (a) Power dependent Stokes and anti-Stokes Raman spectra of SMO film at 150 K with a 532-nm laser source. (b) Power-dependent Stokes and anti-Stokes Raman spectra of SMO film at 300 K with a 532-nm laser source. (c) Temperature-dependent Stokes and anti-Stokes Raman spectra with a 1.69-mW laser source (532 nm).

and 300 K is similar to the temperature-dependent shift in A_g mode at a constant laser power. Figure 6(b) represents the variation of the A_g mode with increasing laser power and temperature with a 633-nm laser source. With a 633-nm laser, the power-dependent A_g mode softening takes place

with increasing power, and this trend is similar to the temperature variation of the A_g mode at a fixed laser power. In this case also, we considered the effect of laser heating for temperature-dependent measurements. Measurement at the highest laser power (9.39 mW, 633 nm laser source) at room

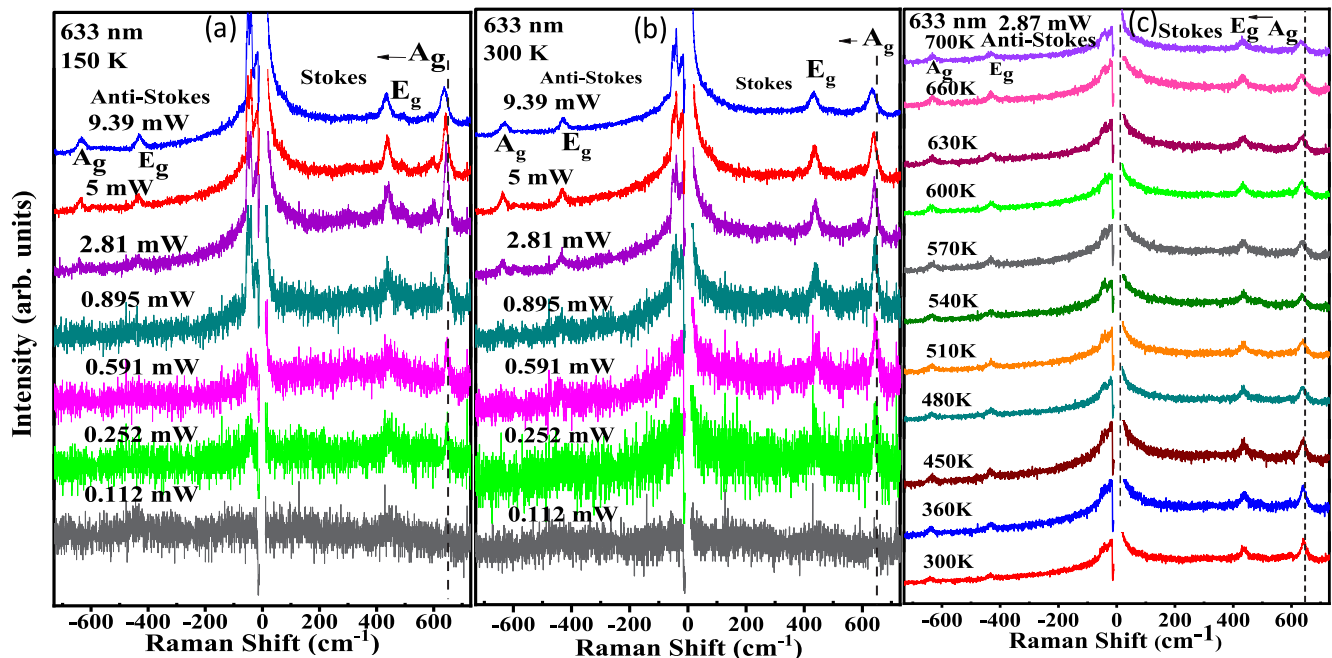


FIG. 5. (a) Power-dependent Stokes and anti-Stokes Raman spectra of SMO film at 150 K with a 633-nm laser source. (b) Power-dependent Stokes and anti-Stokes Raman spectra of SMO film at 300 K with a 633-nm laser source. (c) Temperature-dependent Stokes and anti-Stokes Raman spectra with a 2.87-mW laser source (633 nm).

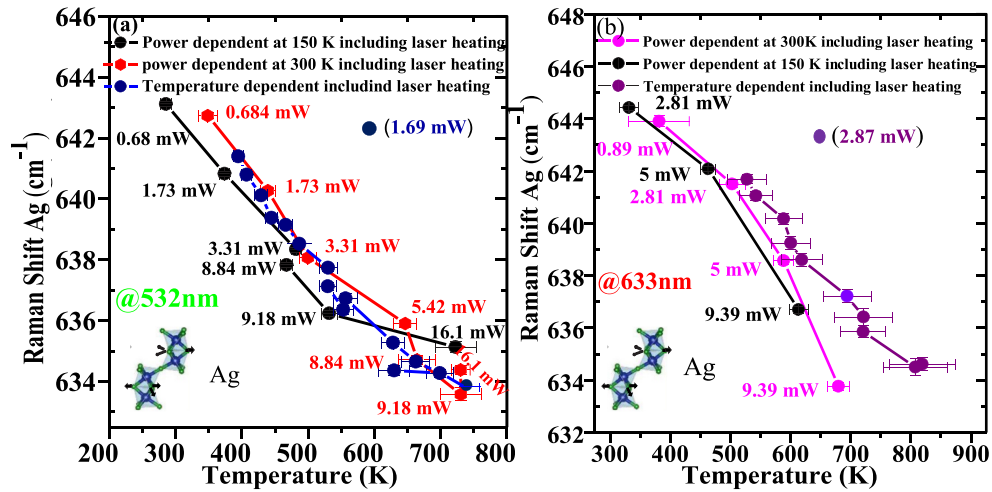


FIG. 6. (a) Power-dependent variation of the A_g mode at 150 K and 300 K, including local temperature, calculated from a Stokes and anti-Stokes ratio, along with temperature variation of the A_g mode at a fixed laser power, including a laser-induced temperature effect for a 532-nm green laser source. (b) Power-dependent variation of the A_g mode at 150 K and 300 K, including local temperature, calculated from a Stokes and anti-Stokes ratio, along with temperature variation of the A_g mode at a fixed laser power, including a laser-induced temperature effect for a 633-nm red laser source.

temperature (300 K) increased local temperature to 690 K [Fig. 6(b)]. Even though a similar trend is observed in power- and temperature-dependent A_g mode softening with respect to local temperature, a considerable deviation is observed with the 633-nm laser source. We also calculated mode softening with respect to laser power and temperature with the 473-nm laser source and the variation looks similar to the 532- and 633-nm laser sources (Supplemental Material Fig. S3 [28]). However, regarding the 473-nm laser source, we were unable to calculate the local temperature effect with increasing laser power. (We were unable to collect the anti-Stokes line by Horiba JY make HR-800 Raman instruments because of the absence of a notch filter.)

It is to be noted that the mode softening with increasing laser power is not the same for all the laser sources (473 nm, 532 nm, and 633 nm). It is observed that with the increase in wavelength, softening of the A_g mode becomes more prominent for the same power; i.e., the A_g mode softening with the 633-nm laser source is higher than the 532-nm laser source for the same laser power (see Supplemental Material Figs. S4 and S5 [28]). In SMO, the 532-nm laser source at 9.18 mW causes a rise in local temperature up to 732 K, whereas the 633-nm laser source radiation at 9.39 mW causes a rise in local temperature up to 680 K. So with comparable power density, 633-nm laser illumination causes a lesser rise in local temperature compared to the 532-nm laser source. This shows that 633-nm laser illumination converts part of its absorber energy better into strain energy in SMO than the 532-nm laser illumination. Therefore, SMO is more photostrictive at a 633-nm illumination. In our 4H-SMO film, the laser-induced local temperature rise is quite high (for this kind of granular surface morphology). Generally, a high number of grain boundaries reduces the effect of local temperature, because most of the absorbed photon energy is absorbed by the free electrons at the grain boundary [32–37], which contributes to the photocurrent as well.

Figure 7(a) represents the Mn- L edge XAS spectra of the grown 4H-SMO film. The $L_{3,2}$ peak arises due to transition from the spin-orbit split Mn $2P_{3/2,1/2}$ to the unoccupied Mn $3d$ state. In Fig. 7(a), we show the Mn- L edge XAS spectra of 4H-SMO with and without laser light illumination (at 532 nm and 633 nm with a power density of 166 mW/mm²). The 4H-SMO Mn- L edge XAS spectrum with a normal and light illumination condition appears similar, with respect to the main peak position, to the reference sample MnO₂, which confirms the Mn⁴⁺ charge state in the grown film. To investigate the charge state and other related changes before and after illumination, we aligned the L_2 position at a fixed energy and observed the scenario of the L_3 edge. A similar L_3 position after and before laser illumination confirms that the charge state of SMO remains invariant after laser illumination. However, a closer inspection reveals that the prepeak at 640.6 eV changes its position and intensity with laser illumination. The origin of the main peak, prepeak, and different features depend on several atomic factors, such as charge state, p - d hybridization, onsite Coulombic correlation, core hole and valence electron Coulomb interactions, hopping parameters, etc. [25,38]. For a better understanding of the origin of shifting of the prepeak, we simulated the Mn- L edge for the 4+ charge state in CTM4-XAS software [38]. Figure 7(b) represents the simulated Mn- L edge for the 4+ charge state. From the simulation, we observe that the prepeak feature strongly depends on the F_{dd} parameter. This Slater integral reduction in the Hartree-Fock value (F_{dd}) defines the Mn $3d$ valance and $2p$ core interaction strength. During the simulation, onsite Coulomb repulsion energy ($U_{dd} = 4.5$ eV) and charge transfer energy ($\Delta = 4.5$ eV, experimentally measured by resonant photoemission spectroscopy [39]) were fixed. So it is divulged that, with the laser illumination, though the charge state of SMO remains the same (Mn⁴⁺), the $2p$ - $3d$ hybridization strength is modified through local distortion.

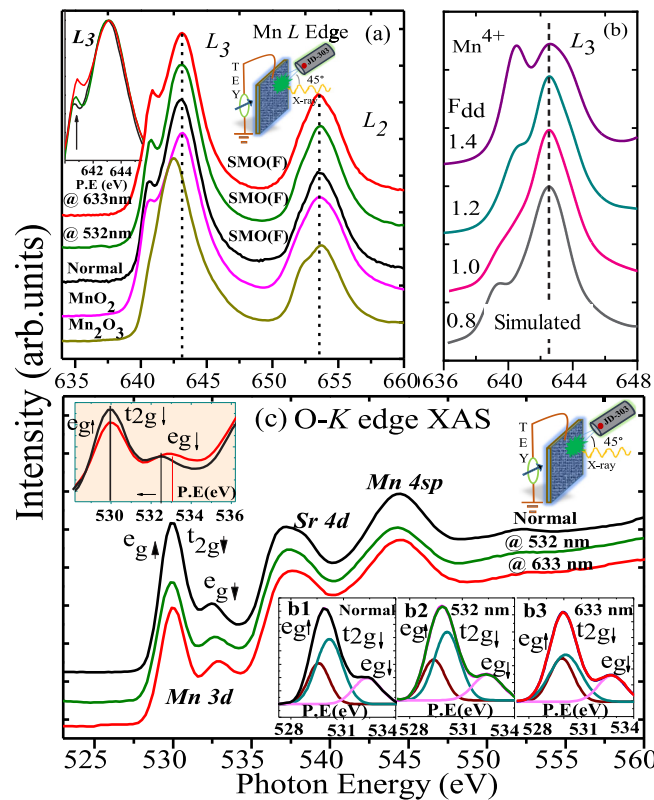


FIG. 7. (a) Mn-L edge XAS spectra of grown SMO, 532-nm laser illuminated SMO, 633-nm laser illuminated SMO film with MnO_2 and Mn_2O_3 reference sample. The inset (right) represents a schematic of XAS measurements with laser illuminations, left inset figure represents zoom view of L3 edge. (b). Simulated spectra of the Mn-L edge for the 4+ charge state with a different Hartree-Fock parameter F_{dd} value. (c) O-K edge XAS spectra of SMO film with normal conditions, illumination of 532 nm, and a 633-nm laser source. Inset is the fitted O-K edge with crystal-field splitted t_{2g} and e_g .

To visualize the effect of the laser-induced local strain on the electronic properties of 4H-SMO film, we performed XAS (O-K edge) measurements in the presence of 532-nm and 633-nm laser sources, as shown in Fig. 7(c). The O-K edge spectrum arises due to the transition between O 1s to O 2p, which is hybridized with Mn 3d states. Thus, the O-K edge contains information about O 2p and Mn 3d hybridization, along with the unoccupied states of Mn 3d. The first two features in the O-K edge are attributed to the hybridization of Mn 3d with O 2p. Higher energy features are due to the hybridization of O 2p with Sr 4d and Mn 4sp, respectively. The first peak in the O-K edge arises due to combined $e_g \uparrow$ and $t_{2g} \downarrow$ states, and the feature at around 533 eV corresponds to $e_g \downarrow$ [40]. These features in the O-K edge are very sensitive with respect to local distortion-mediated change in p -d hybridization or change in stoichiometry [25].

To compare the changes in the electronic structure upon laser illumination, we align the first feature of the O-K edge of all three normalized spectra at the same energy position and examine the second $e_g \downarrow$ feature position. It is observed that while illuminating SMO film with a laser source, the $e_g \downarrow$

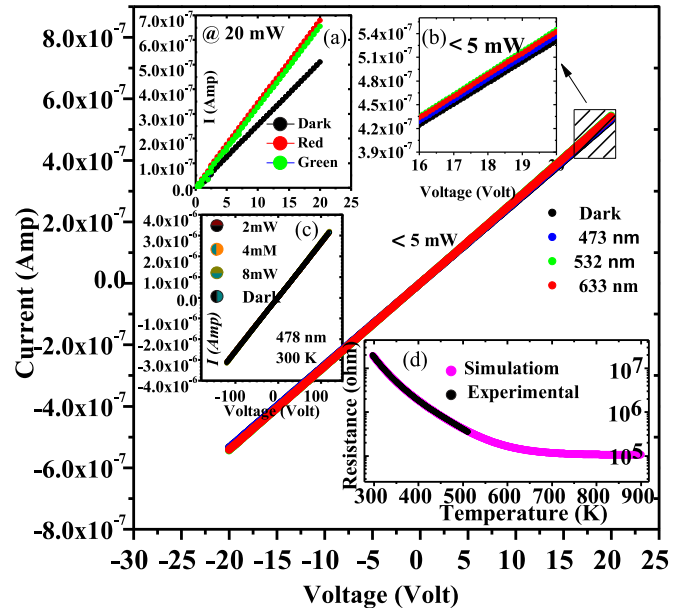


FIG. 8. Room-temperature (300 K) I-V in the presence of a 473-nm, 532-nm, and 633-nm laser source below 5 mW of laser power. (a) Room-temperature (300 K) I-V with a 532-nm and 633-nm laser source with 20 mW of laser power. (b) Zoom view of low-power I-V at a high-voltage regime. (c) Room-temperature (300 K) I-V with 478 nm of laser illumination at different laser power. (d) Variation in resistance of SMO film with temperature along with extrapolated data.

feature shifts toward the higher energy side. When the O-K edge is fitted with the three Gaussian peaks [22], as shown in the inset of Fig. 7(c) (inset b1, b2, b3), we observe the intensity ratio very close to 2:3:2, consistent with the number of unoccupied states in the Mn 3d $e_g \uparrow$, $t_{2g} \downarrow$, and $e_g \downarrow$ states, respectively, of Mn^{4+} ($3d^3$) state. This further confirms that the first three features in the O-K edge spectra account to the Mn 3d $e_g \uparrow$, $t_{2g} \downarrow$, and $e_g \downarrow$ states hybridized with the O 2p orbitals. The crystal field of the 4H-SMO film ($t_{2g} \downarrow - e_g \downarrow$) with the normal condition is 2.2 eV, while with 532-nm and 633-nm illuminations, crystal field values are 2.5 eV and 2.7 eV, respectively. The local crystal field and effective density of state of 4H-SMO are highly sensitive to local distortion-mediated change in p -d hybridization [24,25]. We also noticed light-induced changes in the local structure (from the blue shift of the A_g mode upon light illumination) modifying the crystal field and effective p -d hybridization in this compound.

So far, it is evident that the 4H-SMO thin film generates a huge local temperature rise upon laser light illumination. However, it needs to be determined whether all the absorbed photon energy is spent in local heating or whether some part of the absorbed photon energy is participating in the electron transport mechanism! To address this issue, we performed photocurrent measurements with different laser sources with different powers, along with the temperature-dependent resistivity measurements. Figure 8 represents a room-temperature (300 K) current-voltage (I-V) plot of SMO film with a 478 nm, 532-nm, and 633-nm light source, with power less than 5 mW. No such photocurrent is observed for any

wavelength with this low-power laser, even at higher voltages [see inset in Fig. 8(b)]. With the 478 nm light source [Fig. 8(c)] at up to 8 mW of laser power, we do not observe any enhancement in photocurrent. However, with the 533-nm and 633-nm laser sources, we observed enhancement in photocurrent as estimated with the help of I-V measurements at 20-mW laser power [Fig. 8(a)]. From the Raman study, it is observed that the 4H-SMO local temperature increases when a high, intense laser source is illuminated. Thus, the local temperature-mediated change in resistivity may be the cause of the enhancement in the photocurrent in 4H-SMO film. For that purpose, we performed high-temperature (up to 515 K) resistivity measurement of 4H-SMO film and extrapolated the data for higher temperature values. Figure 8(d) shows resistance versus temperature of grown SMO film, which reveals a decrease in resistance with increasing temperature. So, an increase in photocurrent with a high-power laser source is mainly due to a decrease in resistivity with an increase in local temperature.

III. DISCUSSION

In this work, we observed that 4H-SMO interacts with a broad optical frequency range. The local structure of 4H-SMO is also modified while interacting with light, resulting in changes in its crystal field and p - d hybridization. From the Raman Stokes and anti-Stokes ratio, we observed a huge local temperature enhancement during laser illumination. Illumination from a 532-nm laser at a laser power of 9.18 mW causes an increase in local temperature up to 740 K, while 633-nm laser illumination at 9.38 mW of laser power increases the local temperature to around 690 K. So, at comparable laser power illumination, red light induced a relatively smaller local temperature rise with respect to the green laser. We analyzed temperature-dependent Raman spectra at a fixed laser power, and power dependence at a fixed temperature, and they show similar variations in vibrational modes. With 532-nm laser source illumination, power-dependent mode variation at different temperatures, and temperature-dependent variation of Raman mode at a fixed power follow exactly the same path. On the other hand, with the 633-nm red laser source, though softening of the A_g mode is observed with the laser power as well as temperature variation, the trend of softening with the laser power and temperature does not follow each other and is slightly deviated. The mode softening with the 633-nm laser is relatively large with respect to the 532-nm laser source. In photoconductivity measurements, we observed the highest conductivity with the 633-nm laser source. So possibly 4H-SMO converts some portion of photon energy directly into mechanical energy of 633-nm red light. Generally, photostriction in other perovskite systems—for example, a single crystal of BiFeO₃, takes place through the UV and visible range, where the band gap lies in the visible light energy range [41]. However, in this work we observed the photosensing phenomena even for laser energy values lower than the band gap of 4H-SMO. We performed room-temperature Raman measurements with a 532-nm laser source at 1.5 mW of laser power and then performed Raman measurements at

15 mW of laser power; after that, we again performed the same experiment with a 1.5-mW laser source. We observed that the mode position observed with 15 mW of laser power returned to its initial position when illuminated subsequently with 1.5 mW of laser power (see the most intense A_g mode in Supplemental Material Fig. S9 [28]). This shows that the laser-induced softening can be easily recovered by switching off the optical excitation.

IV. CONCLUSION

We have successfully grown stoichiometric 4H-SMO thin film on an optically transparent quartz substrate. From power-dependent Raman measurements, it is confirmed that the local structure of this SMO thin film is modified with increasing laser power, and local structure modification with 9 mW of laser illumination (at 532 nm and 633 nm) is similar to 1.2% substrate-induced distortion in this structure. From our Raman Stokes and anti-Stokes measurements, we observed a high local temperature rise; for instance, the local temperature at 300 K is enhanced to 700 K when illuminated with a 532-nm laser source at 9 mW. In a correlated perovskite system, this high temperature rise is rare, particularly for a granular morphic structure. Mode variation with respect to power and temperature is very similar for the 532-nm laser source, while it is slightly diverted for the 633-nm laser source. At the same time, we observed a maximum photocurrent with the 633-nm light source. By definition, photostriction must be a nonthermal phenomenon. On this basis, BiFeO₃ is considered a photostrictive material. However, a very recent report [7] claims that during laser illumination, the local temperature (from the Stokes-to-anti-Stokes ratio) in BiFeO₃ also increases greatly, and domain structure variation in epitaxial BiFeO₃ with laser light at a fixed temperature and with temperature variation at a fixed laser light source are similar. Even giant photostrictive SrIrO₃ thin film also shows temperature-dependent structural distortion. So local temperature measurements in all such cases are a debatable issue [42,43]. We propose 4H-SMO as a photosensitive material. Even in a granular relaxed structure, it generates huge local temperatures throughout the entire optical range, and local distortion increases toward the infrared regime. Our findings will help us to explore this system as a solar power heater, as a local thermal insulating materials for thermal energy storage, as noncontact infrared thermometer, and as a backlit display material in the future.

ACKNOWLEDGMENTS

S.S. acknowledges the funding from SERB (No. CRG/2019/002668), India. A.J. acknowledges CSIR [CSIR File No. 09/1020(0179)/2019-EMR-I] for the research grant.

The authors thank Dr. V. R. Reddy for GIXRD and XRR measurements. They also thank Dr. Subhabrata Dhar for photoconductivity measurements, Dr. R. Venkatesh and Mr. Mohan Gangrade for AFM measurements, and Mr. Rakesh Shah and A. Wadikar for XAS measurements. The authors acknowledge Parveen, Suman, and Satish for their technical support.

- [1] R. Ramesh and N. A. Spaldin, *Nat. Mater.* **6**, 21 (2007).
- [2] J. Ma, J. Hu, Z. Li, and C. W. Nan, *Adv. Mater.* **23**, 1062 (2011).
- [3] N. Balke, S. Choudhury, S. Jesse, M. Huijben, Y. H. Chu, A. P. Baddorf, L. Q. Chen, R. Ramesh, and S. V. Kalinin, *Nat. Nanotechnol.* **4**, 868 (2009).
- [4] A. F. Th. Hoekstra, A. S. Roy, T. F. Rosenbaum, R. Griessen, R. J. Wijngaarden, and N. J. Koeman, *Phys. Rev. Lett.* **86**, 5349 (2001).
- [5] V. Iurchuk, D. Schick, J. Bran, D. Colson, A. Forget, D. Halley, A. Koc, M. Reinhardt, C. Kwamen, N. A. Morley, M. Bargheer, M. Viret, R. Gumeniuk, G. Schmerber, B. Doudin, and B. Kundys, *Phys. Rev. Lett.* **117**, 107403 (2016).
- [6] B. Kundys, M. Viret, D. Colson, and D. O. Kundys, *Nat. Mater.* **9**, 803 (2010).
- [7] Y.-D. Liou, Y.-Y. Chiu, R. T. Hart, C.-Y. Kuo, Y.-L. Huang, Y.-C. Wu, R. V. Chopedakar, H.-J. Liu, A. Tanaka, C.-T. Chen, C.-F. Chang, L. H. Tjeng, Y. Cao, V. Nagarajan, Y.-H. Chu, Y.-C. Chen, and J.-C. Yang, *Nat. Mater.* **18**, 580 (2019).
- [8] J.-C. Yang, Y.-D. Liou, W.-Y. Tzeng, H.-J. Liu, Y.-W. Chang, P.-H. Xiang, Z. Zhang, C.-G. Duan, C.-W. Luo, Y.-C. Chen, and Y.-H. Chu, *Nano Lett.* **18**, 7742 (2018).
- [9] D. Daranciang *et al.*, *Phys. Rev. Lett.* **108**, 087601 (2012).
- [10] C. Chen and Z. Yi, *Adv. Funct. Mater.* **31**, 2010706 (2021).
- [11] T.-C. Wei, H.-P. Wang, H.-J. Liu, D.-S. Tsai, J.-J. Ke, C.-L. Wu, Y.-P. Yin, Q. Zhan, G.-R. Lin, Y.-H. Chu, and J.-H. He, *Nat. Commun.* **8**, 15018 (2017).
- [12] F. Rubio-Marcos, D. Paez-Margarit, A. Ochoa, A. Del Campo, J. F. Fernandez, and J. E. García, *ACS Appl. Mater. Interfaces* **11**, 13921, (2019).
- [13] V. Dwij, B. K. De, S. Rana, H. S. Kunwar, S. Yadav, S. R. Sahu, R. Venkatesh, N. P. Lalla, D. M. Phase, D. K. Shukla, and V. G. Sathe, *Phys. Rev. B* **105**, 134103 (2022).
- [14] Y. Zhou, L. You, S. Wang, Z. Ku, H. Fan, D. Schmidt, A. Rusydi, L. Chang, P. R. Le Wang, L. Chen, G. Yuan, L. Chen, and J. Wang, *Nat. Commun.* **7**, 11193 (2016).
- [15] X. Li, C. Chen, F. Zhang, X. Huang, and Y. Zhiguo, *Appl. Phys. Lett.* **116**, 112901 (2020).
- [16] Y. Li, C. Adamo, P. Chen, P. G. Evans, S. M. Nakhmanson, W. Parker, C. E. Rowland, R. D. Schaller, D. G. Schlom, D. A. Walko, H. Wen, and Q. Zhang, *Sci. Rep.* **5**, 16650 (2015).
- [17] V. Juvé, R. Gu, S. Gable, T. Maroutian, G. Vaudel, S. Matzen, N. Chigarev, S. Raetz, V. E. Gusev, M. Viret, A. Jarnac, C. Laulhé, A. A. Maznev, B. Dkhil, and P. Ruello, *Phys. Rev. B* **102**, 220303(R) (2020).
- [18] H. Wen, M. Sassi, Z. Luo, C. Adamo, D. G. Schlom, K. M. Rosso, and X. Zhang, *Sci. Rep.* **5**, 15098 (2015).
- [19] S. Pal, A. Bihari Swain, P. Parimal Biswas, and P. Murugavel, *Phys. Rev. Materials* **4**, 064415 (2020).
- [20] B. Zhang, X. He, J. Zhao, C. Yu, H. Wen, S. Meng, E. Bousquet, Y. Li, C. Ge, K. Jin, Y. Tao, and H. Guo, *Phys. Rev. B* **100**, 144201 (2019).
- [21] X. Miao, T. Qiu, S. Zhang, H. Ma, Y. Hu, and F. B. Z. Wu, *J. Mater. Chem. C* **5**, 4931 (2017).
- [22] C. Becher, L. Maurel, U. Aschauer, M. Lilienblum, C. Magén, D. Meier, E. Langenberg, M. Trassin, J. Blasco, I. P. Krug, P. A. Algarabel, N. A. Spaldin, J. A. Pardo, and M. Fiebig, *Nat. Nanotechnol.* **10**, 661 (2015).
- [23] R. Guzman, L. Maurel, E. Langenberg, A. R. Lupini, P. A. Algarabel, J. A. Pardo, and C. Magen, *Nano Lett.* **16**, 2221 (2016).
- [24] P. Agrawal, J. Guo, P. Yu, C. Hebert, D. Passerone, R. Erni, and M. D. Rossell, *Phys. Rev. B* **94**, 104101 (2016).
- [25] A. K. Mandal, A. Jana, B. K. De, N. Patra, P. Rajput, V. Sathe, S. N. Jha, R. J. Choudhary, and D. M. Phase, *Phys. Rev. B* **103**, 195110 (2021).
- [26] J. H. Lee and K. M. Rabe, *Phys. Rev. Lett.* **104**, 207204 (2010).
- [27] A. Edström and C. Ederer, *Phys. Rev. Lett.* **124**, 167201 (2020).
- [28] See Supplemental Material at <http://link.aps.org/supplemental/10.1103/PhysRevB.106.104104> for crystal structure, surface morphology and time evolution of Raman mode of SMO thin film.
- [29] A. Sacchetti, M. Baldini, F. Crispoldi, P. Postorino, P. Dore, A. Nucara, C. Martin, and A. Maignan, *Phys. Rev. B* **72**, 172407 (2005).
- [30] A. Sacchetti, M. Baldini, P. Postorino, C. Martin, and A. Maignan, *J. Raman Spectrosc.* **37**, 591 (2006).
- [31] R. Søndénå, S. Stølen, and P. Ravindran, *Phys. Rev. B* **75**, 214307 (2007).
- [32] J. Seide, D. Fu, S.-Y. Yang, E. Alarcón-Llado, J. Wu, R. Ramesh, and J. W. Ager III, *Phys. Rev. Lett.* **107**, 126805 (2011).
- [33] S. Körbel and S. Sanvito, *Phys. Rev. B* **102**, 081304(R) (2020).
- [34] N. Faraji, C. Ulrich, N. Wolff, L. Kienle, R. Adelung, Y. Kumar Mishra, and J. Seidel, *Adv. Electron. Mater.* **2**, 1600138 (2016).
- [35] S. Nandy, P. S. V. Mocherla, K. Kaur, S. Gautam, B. R. K. Nanda, and C. Sudakar, *J. Appl. Phys.* **126**, 235101 (2019).
- [36] Z. Chu, M. Yang, P. Schulz, D. Wu, X. Ma, E. Seifert, L. Sun, X. Li, K. Zhu, and K. Lai, *Nat. Commun.* **8**, 2230 (2017).
- [37] N. Sarkar, S. Dhar, and S. Ghosh, *J. Phys.: Condens. Matter* **15**, 7325 (2003).
- [38] E. Stavitski and F. M. F. de Groot, *Micron* **41**, 687 (2010).
- [39] A. Kumar Mandal, A. Jana, S. Chowdhury, A. Tiwari, R. J. Choudhary, and D. M. Phase, *J. Phys.: Condens. Matter* **33**, 235501 (2021).
- [40] D. Bauernfeind, R. Triebl, M. Zing, M. Aichhorn, and H. G. Evertz, *Phys. Rev. B* **97**, 115156 (2018).
- [41] B. Kundys, M. Viret, C. Meny, V. Da Costa, D. Colson, and B. Doudin, *Phys. Rev. B* **85**, 092301 (2012).
- [42] A. Ahlawat and V. G. Sathe, *J. Raman Spectrosc.* **42**, 1087 (2011).
- [43] A. Laikhtman and A. Hoffman, *J. Appl. Phys.* **82**, 243 (1997).